

# Modeling scattering from lightning-induced ionospheric disturbances with the discontinuous Galerkin method

F. R. Foust,<sup>1</sup> M. Spasojevic,<sup>1</sup> T. F. Bell,<sup>1</sup> and U. S. Inan<sup>1,2</sup>

Received 1 July 2011; revised 15 September 2011; accepted 21 September 2011; published 2 December 2011.

[1] Simulation of the propagation of very low frequency (VLF) waves in the Earth-ionosphere waveguide remains a significant computational challenge as a result of the variable wavelength at these frequencies in the magnetized plasma environment of the lower ionosphere. The discontinuous Galerkin (DG) method is naturally and easily adapted to nonuniform grids and so is ideal for simulation in media where the characteristic length scale varies significantly. We present an automatic procedure based on minimal system realization to incorporate any linear, anisotropic dispersive material in the DG framework, with application to a perfectly matched layer and scattering from strong disturbances in a magnetoplasma. We apply these techniques to modeling of scattering from lightning electromagnetic pulse-induced ionospheric disturbances, calculating the full 3-D scattered VLF wavefields from intense lightning-induced ionospheric perturbations over a large volume. We plot the spatial distribution of the phase and amplitude response as seen by a ground-based receiver over a large area. The results are consistent with previous results from 2-D models, showing maximum received signal strength amplitude perturbations on the order of 0.1 to 0.2 dB for intense vertical discharges under smooth ambient conditions and on the order of 0.5 dB for very intense, repeated horizontal discharges.

**Citation:** Foust, F. R., M. Spasojevic, T. F. Bell, and U. S. Inan (2011), Modeling scattering from lightning-induced ionospheric disturbances with the discontinuous Galerkin method, *J. Geophys. Res.*, 116, A12301, doi:10.1029/2011JA016973.

## 1. Introduction

[2] Modeling very low frequency (VLF, 3–30 kHz) wave propagation in the Earth-ionosphere waveguide remains an important yet computationally difficult problem. In free space, VLF waves have typical wavelengths in the range of tens of kilometers. However, the situation rapidly changes in the partially ionized lower ionosphere. Near the VLF reflection height (approximately 85 km at night) for a typical midlatitude ionosphere at 24 kHz, the wavelength can drop to less than a quarter of its free-space value for propagation parallel to the background magnetic field or even zero for non-parallel propagation [Stix, 1962]. There have been many approaches to modeling propagation and scattering of VLF waves in the Earth-ionosphere waveguide. Some full-wave models solve a series of one-dimensional reflection problems at the boundaries between uniform, stratified layers and then use these reflection coefficients to find the solution to arbitrary problems as the sum of waves in  $k$ -space. Such techniques have been used to successfully model propagation of VLF waves over very large distances [Pappert and Ferguson, 1986; Lehtinen and Inan, 2008]. Inhomogeneities can be handled in a number of different ways. Modal techniques such as those used by the long-wave propagation

capability (LWPC) [Pappert and Ferguson, 1986] solve for propagation within “slabs,” each of which is assumed to be composed of horizontally stratified layers, infinite in extent. Mode-coupling calculations are used to propagate the fields in each slab into adjacent slabs. Weak, localized disturbances can be handled as done by Lehtinen *et al.* [2010], who uses the Born approximation to model the inhomogeneity as a set of equivalent currents. This approach is powerful but is limited to relatively mild density perturbations. Recently, generic field solvers like finite difference time domain (FDTD) [Taflove and Hagness, 2005; Yee, 1966] have gained in popularity and have been successfully applied to VLF propagation and scattering off ionospheric disturbances [Cummer, 2000; Peter *et al.*, 2006; Marshall and Inan, 2010]. These simulations are typically bound by the number of unknowns required to accurately discretize the space. Typical rule-of-thumb guidelines state that on the order of 10 cells per wavelength are required to accurately represent a solution using FDTD [Taflove and Hagness, 2005, p. 34]. While this is not necessarily prohibitive for moderately-sized problems (on the order of a few hundred kilometers per spatial dimension) within the Earth-ionosphere waveguide, the situation rapidly degrades above the VLF reflection height, where the wavelength can easily drop to less than a quarter of its free space value. For reasonable accuracy on a fixed FDTD grid, then, the grid spacing must be chosen on the basis of the smallest wavelength of interest in the solution, and thus is enormously prohibitive. While FDTD can be used on semi-structured (plaid) and even fully

<sup>1</sup>Department of Electrical Engineering, Stanford University, Stanford, California, USA.

<sup>2</sup>Electrical Engineering Department, Koç University, Istanbul, Turkey.

unstructured grids, doing so typically reduces the formal order of accuracy of the scheme from second to first order, and also significantly complicates the derivation of current update equations for magnetized plasmas or other anisotropic, dispersive materials. High-order FDTD techniques, by contrast, suffer from non-locality of the finite difference operators, which leads to failure of the scheme in the presence of sharp gradients or material discontinuities.

[3] In this paper, we discuss the application of a relatively new class of techniques known as nodal discontinuous Galerkin (DG) methods to the problem of wave propagation in the Earth-ionosphere waveguide. Since it is straightforward to use the DG method on unstructured grids and doing so has no impact on the formal order of accuracy, we can manage the scale problem by sampling more finely only where it is needed, i.e., near the VLF reflection height, while using a coarser grid elsewhere. This approach allows accurate and flexible simulation of scattering off ionospheric disturbances in the VLF regime with fewer restrictions on the type or magnitudes of the plasma density perturbations that can be modeled.

### 1.1. Background

[4] Lightning discharges can modify the ionosphere via a number of different mechanisms. Because of the impulsive, energetic nature of a lightning return stroke, a large electromagnetic pulse (EMP) is radiated from a lightning channel. The fields associated with this EMP are intense enough to cause significant heating and ionization of the ionosphere above the discharge [Inan et al., 1991; Cheng et al., 2007; Marshall et al., 2008, 2010]. A number of secondary effects are also present; for instance, the amount of charge removed by a lightning return stroke creates a large quasi-electrostatic (QE) field above a lightning discharge, which can further modify the levels of ionization [Pasko et al., 1995, 1998]. In either the QE case or the EMP case, the magnitude of the change in the ambient electron density can be on the order of a few percent to over a hundred percent, peaking in an altitude range of approximately 80 to 100 km and extending over radial distances of over 100 km [Cheng et al., 2007; Marshall et al., 2010]. Because of the abrupt onset of such disturbances, their altitudes near the VLF reflection height, and their relatively wide spatial extent, they are expected to modify the properties of VLF waves propagating within the Earth-ionosphere waveguide. This can be observed by a ground-based receiver as a phase or magnitude perturbation on a received narrowband signal observed shortly after a causative lightning discharge. Indeed, this connection was observed quite early [Armstrong, 1983], but the exact nature of the disturbances and their effects on received VLF signals have not yet been fully resolved.

[5] We discuss one particular class of VLF signal disturbances, termed “early” VLF events. Early VLF events are abrupt changes in the amplitude of a received narrowband VLF signal following a lightning discharge. They are characterized by their abrupt onset ( $< 20$  ms) after a causative lightning discharge (hence the term “early”) and their relatively slow recovery time (10–100 s). Early/fast VLF events are also characterized by 15 dB beam widths of less than  $20^{\circ}$ – $30^{\circ}$  [Johnson et al., 1999; Moore et al., 2003]. A number of different causative mechanisms have been postulated [Inan et al., 1991; Pasko et al., 1998; Moore

et al., 2003]. More recent modeling efforts have focused on EMP-induced ionospheric disturbances and shown that they are not inconsistent with such events [Cheng and Cummer, 2005; Cheng et al., 2007; Marshall and Inan, 2010]. A recent survey paper [Inan et al., 2010] summarizes what is known (as of 2010) of these lightning-ionosphere interactions, among others. Recent modeling efforts by Cheng and Cummer [2005], Cheng et al. [2007], and Marshall and Inan [2010] have focused on scattering from lightning EMP-induced ionospheric disturbances, which we investigate further in this paper.

[6] We compute the narrowband VLF fields scattered from such lightning EMP-induced density perturbations. Previous work by Marshall and Inan [2010] used a 2-D finite difference model to show that the EMP from very intense lightning discharges, with  $E_{100}$  (defined by Uman and McLain [1970] as the magnitude of the electric field as observed on the ground at 100 km from a discharge) in the range of 7–40 V/m, can perturb the ambient electron density enough to cause measurable perturbations on the amplitude of a received narrowband VLF signal. Later work by Lehtinen et al. [2010] used the Born approximation to approximate the scattered field in a medium of homogeneous, horizontally stratified layers. This work revealed the full three-dimensional structure of the scattered field from a lightning EMP-induced density perturbation for a range of incidence angles. The technique used by Lehtinen et al. [2010], however, assumes that the scattered field is much smaller than the incident field and as such is unsuitable for the whole range of density perturbations considered by Marshall and Inan [2010]. In addition, the technique cannot account for multiple scattering or modes propagating exactly parallel to the stratified layers, necessitating the use of a more general solution method for strong perturbations. The magnitude, angular extent, and shape of the scattered field and amount of transverse variation for intense, spatially complicated (e.g., ring-shaped) disturbances were previously unknown; this work seeks to address this.

[7] We extend the work of Lehtinen et al. [2010] and Marshall and Inan [2010], using a fully three-dimensional continuum electromagnetic DG solver to solve for the VLF scattered fields from an EMP-induced ionospheric disturbance. The DG method has an arbitrary order of accuracy but is also highly local and parallelizable, combining desirable features from the finite element method and the finite volume method. Similar to low-order finite volume methods, the only data that must be communicated between CPUs are the field values at the faces between elements. In contrast to traditional finite element methods, the mass matrices are strictly local to each element; thus, no large, sparse system of equations need be solved. In addition, the polynomial order (and thus the accuracy) can be increased as much as desired without increasing the physical width of the stencil or destroying the locality of the scheme. As a continuum, time domain method, backscattering and multiple scattering are implicitly handled; the only significant limitation, similar to those in FDTD techniques, is that the wavelengths of interest must be sufficiently sampled. For traditional staggered-grid FDTD, a minimum 2 cells per wavelength are required for convergence, but typical rule-of-thumb guidelines dictate that on the order of 10 cells per wavelength are required for acceptable accuracy. The DG method has similar

restrictions: at minimum, on the order of  $\pi$  unknowns per wavelength are required for convergence. However, in contrast to FDTD, the order of accuracy can be increased without restrictions on the material parameters or the amount of grid inhomogeneity. This means that for a given domain, the error in a high-order DG simulation will decrease faster than that of an FDTD simulation for a given reduction in the grid size. Further, the DG technique is easily adapted for use on completely unstructured, strongly inhomogeneous meshes, which allows us to use smaller cells only where they are needed, e.g., in the ionosphere where the VLF whistler wavelengths are much shorter than their free-space equivalents for a given frequency. In the context of this simulation work, the free-space wavelength is equal to 12.5 km, but in the ionosphere drops to less than 2 km for propagation parallel to the magnetic field.

## 1.2. Outline and Summary

[8] We begin by discussing the computational model in section 2. We show how to incorporate linear, anisotropic dispersive materials, applying the technique to the cold plasma model used in this paper and to the perfectly matched layer (PML), an absorbing boundary first introduced by *Berenger* [1994], we use to truncate part of the domain for our simulations. We validate the technique in section 3, showing that the scheme is consistent with analytical results. We discuss the ambient model, scattering model, computational domain, and source conditions in section 4. In section 5, we discuss the results, showing the scattered field amplitudes on the ground for a variety of incident source conditions.

[9] Our three-dimensional simulation results show that the scattered fields from lightning EMP-induced ionospheric disturbances can have complicated structure with strong transverse variation, particularly in the region near a disturbance produced by a vertical lightning discharge. Our model shows that while not all features of “early” VLF events can be reproduced by a single, large vertical lighting EMP-induced disturbance, the scattered field amplitudes are nonetheless significant, with measurable amplitude changes greater than 0.2 dB possible under smooth ambient conditions. As an extreme case, we show that the disturbance induced by 60 repeated, intense intercloud lightning discharges can result in strong perturbations on the order of 0.2 to 0.5 dB under smooth ambient conditions, with the near-field values showing strong spatial variation. We also show that while the bulk of the wave energy from such large (with respect to the wavelength) disturbances is scattered in the forward direction, there are nonetheless non-negligible scattered fields in the transverse direction. We also show the phase response from the same simulations, showing that it may also be a useful diagnostic measure when considering narrowband signal perturbations from ionospheric scatterers.

## 2. Methods

### 2.1. Nodal Discontinuous Galerkin Formulation

[10] The nodal discontinuous Galerkin (DG) formulation [*Hesthaven and Warburton*, 2002] approximates the solution on a domain by first approximating the solution local to a single finite element using a basis (typically polynomial) and then connecting that solution to neighboring elements using a numerical flux function. The solution method is

effectively a hybrid between finite volume and finite element techniques. The method begins by approximating a solution  $\mathbf{u}^e(\mathbf{x})$  on an element  $e$  with an interpolating Lagrange polynomial basis  $\phi_j(\mathbf{x})$  as

$$\mathbf{u}^e(\mathbf{x}) \approx \sum_{j=1}^N \mathbf{u}(\mathbf{x}_j) \phi_j^e(\mathbf{x}) \quad (1)$$

Substituting this into the generic conservation law  $\frac{\partial \mathbf{u}}{\partial t} + \nabla \cdot \mathbf{F}(\mathbf{u}) = 0$ , where  $\mathbf{F}$  is a tensor, that is,

$$\nabla \cdot \mathbf{F}(\mathbf{u}) = \frac{\partial}{\partial x} F_x(\mathbf{u}) + \frac{\partial}{\partial y} F_y(\mathbf{u}) + \frac{\partial}{\partial z} F_z(\mathbf{u}) \quad (2)$$

Then substituting equation (1) into the conservation law and integrating by parts twice, we have the strong form of the DG scheme:

$$\int_V \left( \frac{\partial \mathbf{u}^e}{\partial t} + \nabla \cdot \mathbf{F}^e(\mathbf{x}) \right) \phi_i^e(\mathbf{x}) d\mathbf{x} = \oint_S \hat{\mathbf{n}} \cdot (\mathbf{F}^e - \mathbf{F}^*) \phi_i^e(\mathbf{x}) d\mathbf{S} \quad (3)$$

The function  $\mathbf{F}^*$  denotes a numerical flux. For the scheme to be well-posed,  $\mathbf{F}^*$  must typically be chosen in such a way that it combines the fluxes interior to an element ( $\mathbf{F}^-$ ) and exterior to an element ( $\mathbf{F}^+$ ) in a physically self-consistent way. For Maxwell's equations, we have [*Hesthaven and Warburton*, 2007]

$$\begin{aligned} M \frac{\partial(\epsilon \mathbf{E})}{\partial t} + S \mathbf{F}_E + M \mathbf{J} &= \oint_S \hat{\mathbf{n}} \cdot (\mathbf{F}_E - \mathbf{F}_E^*) \phi_i(\mathbf{x}) d\mathbf{S} \\ M \frac{\partial(\mu \mathbf{H})}{\partial t} + S \mathbf{F}_H + M \mathbf{J}_m &= \oint_S \hat{\mathbf{n}} \cdot (\mathbf{F}_H - \mathbf{F}_H^*) \phi_i(\mathbf{x}) d\mathbf{S}, \end{aligned} \quad (4)$$

where we have dropped the superscript  $e$  for clarity, understanding that this is the solution defined only on a single element  $e$ . The terms  $\mathbf{J}$  and  $\mathbf{J}_m$  are the electric and magnetic currents, respectively. The normal at each face of the element is  $\hat{\mathbf{n}}$ . The surface integral terms on the right refer to the integration over all faces of an individual element (a tetrahedron in three dimensions, triangle in two dimensions). The matrices  $M$  and  $S$  are the standard mass and stiffness matrices, respectively:

$$M_{ij} = \int \phi_i(\mathbf{x}) \phi_j(\mathbf{x}) d\mathbf{x} \quad (5)$$

$$S_{ij} = \int \phi_i(\mathbf{x}) \nabla \phi_j(\mathbf{x}) d\mathbf{x} \quad (6)$$

and the fluxes along the normal are

$$\hat{\mathbf{n}} \cdot \mathbf{F}_E = -\hat{\mathbf{n}} \times \mathbf{H}, \quad \hat{\mathbf{n}} \cdot \mathbf{F}_H = \hat{\mathbf{n}} \times \mathbf{E} \quad (7)$$

We use a standard numerical flux as described by *Hesthaven and Warburton* [2007]:

$$\begin{aligned} \hat{\mathbf{n}} \cdot (\mathbf{F}_E - \mathbf{F}_E^*) &= \frac{1}{(Z^+ + Z^-)} (\alpha \hat{\mathbf{n}} \cdot [\mathbf{E}]) - \alpha [\mathbf{E}] - Z^+ \hat{\mathbf{n}} \times [\mathbf{H}] \\ \hat{\mathbf{n}} \cdot (\mathbf{F}_H - \mathbf{F}_H^*) &= \frac{1}{(Y^+ + Y^-)} (\alpha \hat{\mathbf{n}} \cdot [\mathbf{H}]) - \alpha [\mathbf{H}] + Y^+ \hat{\mathbf{n}} \times [\mathbf{E}], \end{aligned}$$

where the plus and minus superscripts denote the field values exterior and interior to the current element, and  $[u] = u^- - u^+$  is the field difference at the face. The parameter  $\alpha$  is variable. Values anywhere between  $\alpha = 0.0$  (full central fluxes) to  $\alpha = 1.0$  (full upwinding) can be used. In practice,

either choice will converge for hyperbolic or weakly hyperbolic systems of equations. In practice, upwinding is generally more accurate and less noisy, but central fluxes will better tolerate a loss of hyperbolicity.

## 2.2. Anisotropic and Dispersive Materials

[11] One key distinguishing feature of the nodal DG method is that the solution is solved at interpolation points, that is, the nodal values are the solution at those points. Thus, the relationship between a current  $\mathbf{J}(\mathbf{x}_i)$  and the associated field  $\mathbf{E}(\mathbf{x}_i)$  at a point  $\mathbf{x}_i$  is direct; no spatial averaging to colocate the fields is required. One way to include arbitrary linear, anisotropic, dispersive materials in the DG framework is to write the relationship between the currents and fields as a set of auxiliary ordinary differential equations defined at each grid point. We now describe a generic procedure for converting a general frequency domain description of such a material into a set of ordinary differential equations.

[12] We begin by noting that any anisotropic permittivity can be represented by an equivalent conductivity tensor via the relation  $\epsilon(\omega) = \epsilon_0(\epsilon_{\infty,r} - \sigma(\omega)/(j\omega\epsilon_0))$ , where we have used the Fourier transform convention  $\partial/\partial t \rightarrow -j\omega$ . The relative permittivity at infinity  $\lim_{\omega \rightarrow \infty} \epsilon_r(\omega) = \epsilon_{\infty,r}$  is simply equal to the unit dyad  $I$  for a physical medium since everything tends to isotropic free space in the high-frequency limit. In a computational setting, however, it is often useful to choose different values. We also note that in a plasma, the conductivities for each species sum, that is,  $\mathbf{J}_{\text{plasma}}(\omega) = \sigma_1(\omega)\mathbf{E}(\omega) + \sigma_2(\omega)\mathbf{E}(\omega) + \dots$ . We wish to rewrite the frequency-dependent relationship  $\mathbf{J}(\omega) = \sigma(\omega)\mathbf{E}(\omega)$  as a first-order ODE such that the ODE has the same frequency response  $\mathbf{J}(\omega)$  for a given input  $\mathbf{E}(\omega)$ :

$$\begin{aligned} \mathbf{x}' &= A\mathbf{x} + B\mathbf{E} \\ \mathbf{J} &= C\mathbf{x} + D\mathbf{E} \end{aligned} \quad (8)$$

For a given system, there may exist an infinite number of matrices  $\{A, B, C, D\}$  that are consistent with the frequency domain description. The task of finding one such set  $\{A, B, C, D\}$  is termed system realization, a well-known problem from control theory. For notational convenience and for consistency with control literature, we now denote the complex frequency  $-j\omega$  as  $s$ . The procedure we use is an SVD-based balanced minimal realization technique discussed by *Antsaklis* [1997]. The first step is to find the minimal polynomial  $m(s)$  of the system, defined as the least common denominator of each entry of the matrix  $\sigma(s)$ . The order of the minimal polynomial is  $r$ .

[13] We begin by writing the frequency dependent conductivity tensor as a series:

$$\sigma(s) = \sigma_0 + \sigma_1 s^{-1} + \sigma_2 s^{-2} + \dots \quad (9)$$

The matrices  $\sigma_0, \sigma_1, \sigma_2, \dots$  are termed the Markov parameters of the system. These can be found as

$$\begin{aligned} \sigma_0 &= \lim_{s \rightarrow \infty} \sigma(s) \\ \sigma_1 &= \lim_{s \rightarrow \infty} s(\sigma(s) - \sigma_0) \\ \sigma_2 &= \lim_{s \rightarrow \infty} s^2(\sigma(s) - \sigma_0 - \sigma_1 s^{-1}) \\ &\dots \end{aligned} \quad (10)$$

Given these Markov parameters, we define the block matrices:

$$K = \begin{bmatrix} \sigma_1 & \dots & \sigma_r \\ \vdots & \ddots & \vdots \\ \sigma_r & \dots & \sigma_{2r-1} \end{bmatrix} \quad (11)$$

$$\hat{K} = \begin{bmatrix} \sigma_2 & \dots & \sigma_{r+1} \\ \vdots & \ddots & \vdots \\ \sigma_{r+1} & \dots & \sigma_{2r} \end{bmatrix} \quad (12)$$

Note that since  $\sigma \in \mathbb{R}^{3 \times 3}$ , both  $K \in \mathbb{R}^{3r \times 3r}$  and  $\hat{K} \in \mathbb{R}^{3r \times 3r}$ . We then find the singular value decomposition (SVD) of the matrix  $K$ :

$$K = [U \quad U_n] \begin{bmatrix} \Sigma & 0 \\ 0 & 0 \end{bmatrix} [V \quad V_n]^T \quad (13)$$

Note that if there are  $n$  nonzero singular values, then  $U \in \mathbb{R}^{3r \times n}$ ,  $\Sigma \in \mathbb{R}^{n \times n}$ , and  $V \in \mathbb{R}^{3r \times n}$ . Note also that we can ignore the zero singular values of  $K$  and equivalently write  $K$  as  $K = U\Sigma V^T$ . A minimal realization of this system is given by

$$\begin{aligned} A &= (\Sigma^{-\frac{1}{2}} U^T) \hat{K} (V \Sigma^{-\frac{1}{2}}) \\ B &= (\Sigma^{\frac{1}{2}} V^T) [I_{3 \times 3} \quad 0_{3 \times (3r-3)}]^T \\ C &= [I_{3 \times 3} \quad 0_{3 \times (3r-3)}] (U \Sigma^{\frac{1}{2}}) \\ D &= \sigma_0 \end{aligned} \quad (14)$$

The matrix  $I_{n \times n}$  denotes the identity matrix of size  $n$ . The matrix  $0_{m \times n}$  denotes the matrix of all zeros of size  $m \times n$ . The resulting matrices are of size:  $A \in \mathbb{R}^{n \times n}$ ,  $B \in \mathbb{R}^{n \times 3}$ ,  $C \in \mathbb{R}^{3 \times n}$ , and  $D \in \mathbb{R}^{3 \times 3}$ .

[14] This particular realization is minimal, meaning that the state vector  $x$  is as small as possible for the given system. In other words, there only exist as many state variables as there are independent degrees of freedom. Further, it is balanced, which means that it is roughly as observable as it is controllable [Gilbert, 1963]. We find that this particular realization method leads to stable, numerically well-behaved schemes. In addition, SVD-based techniques are efficient and easily automated using the LAPACK library, facilitating their incorporation into a generic code. This particular realization, however, is not unique; there exist an infinite number of such matrices  $\{A, B, C, D\}$  and many such algorithms to find them [Ho and Kalman, 1966; Schutter and Moor, 1995; Antsaklis, 1997; Chen, 1999; Schutter, 2000]. Depending on the application, different realizations may have more desirable properties, such as sparsity in the state transition matrix  $A$  or in the mixing matrices  $B$  and  $C$ . Further, in certain materials it may be possible to exploit symmetry in the system to reduce the number of storage variables or number of computations. Any of these adaptations, however, can be easily considered as special cases of the above; for instance, similarity transforms or rotations can be used to transform an existing system into other equivalent forms.

[15] This procedure can be used to generically include any sort of linear, dispersive, anisotropic material in the DG framework. We now show how the technique can be applied to magnetized plasmas and the perfectly matched layer (PML).

### 2.3. Application to a Magnetized Plasma

[16] We first show how this technique can be applied to magnetized plasmas. We begin by writing the first-order ODE governing the relationship between the current  $\mathbf{J}$  for the  $j$ th cold plasma species and the electric field:

$$\begin{aligned} \frac{\partial \mathbf{J}}{\partial t} + \nu \mathbf{J} &= \epsilon_0 \omega_p^2 \mathbf{E} - \boldsymbol{\omega}_c \times \mathbf{J} \\ \omega_p^2 &= \frac{Nq^2}{m\epsilon_0} \\ \omega_c &= \frac{q\mathbf{B}_0}{m} \end{aligned} \quad (15)$$

In the above,  $q$  is the signed charge,  $\omega_p$  is the plasma frequency,  $\nu$  is the effective collision frequency, and the vector  $\boldsymbol{\omega}_c = (\omega_{cx}, \omega_{cy}, \omega_{cz})$  is the signed gyrofrequency vector. Each of the parameters  $q$ ,  $\nu$ ,  $\omega_c$ ,  $\omega_p$  and  $m$  are for a specific plasma species  $j$ . Making the substitution  $\partial/\partial t \rightarrow s$ , we have the matrix equation:

$$\begin{bmatrix} s + \nu & -\omega_{cz} & \omega_{cy} \\ \omega_{cz} & s + \nu & -\omega_{cx} \\ -\omega_{cy} & \omega_{cx} & s + \nu \end{bmatrix} \mathbf{J} = \epsilon_0 \omega_p^2 \mathbf{E} \quad (16)$$

Symbolically inverting this matrix yields a conductivity tensor relating  $\mathbf{J}$  and  $\mathbf{E}$  via  $\mathbf{J} = \boldsymbol{\sigma} \mathbf{E}$ , where each entry is a ratio of polynomials in  $s$ :

$$\begin{aligned} \sigma_j(s) &= \frac{\epsilon_0 \omega_p^2}{d(s)} \begin{bmatrix} \sigma_{xx}(s) & \sigma_{xy}(s) & \sigma_{xz}(s) \\ \sigma_{yx}(s) & \sigma_{yy}(s) & \sigma_{yz}(s) \\ \sigma_{zx}(s) & \sigma_{zy}(s) & \sigma_{zz}(s) \end{bmatrix} \\ \sigma_{xx}(s) &= s^2 + 2\nu s + \nu^2 + \omega_{cx}^2 \\ \sigma_{xy}(s) &= \omega_{cz}s + \omega_{cx}\omega_{cy} + \nu\omega_{cz} \\ \sigma_{xz}(s) &= -\omega_{cy}s - \nu\omega_{cy} + \omega_{cx}\omega_{cz} \\ \sigma_{yx}(s) &= -\omega_{cz}s + \omega_{cx}\omega_{cy} - \nu\omega_{cz} \\ \sigma_{yy}(s) &= s^2 + 2\nu s + \nu^2 + \omega_{cy}^2 \\ \sigma_{yz}(s) &= \omega_{cx}s + \nu\omega_{cx} + \omega_{cy}\omega_{cz} \\ \sigma_{zx}(s) &= \omega_{cy}s + \nu\omega_{cy} + \omega_{cx}\omega_{cz} \\ \sigma_{zy}(s) &= -\omega_{cx}s - \nu\omega_{cx} + \omega_{cy}\omega_{cz} \\ \sigma_{zz}(s) &= s^2 + 2\nu s + \nu^2 + \omega_{cz}^2 \\ d(s) &= (s + \nu)(s^2 + 2s\nu + \nu^2 + |\omega_c|^2) \end{aligned} \quad (17)$$

In practice, we have found that the Hankel matrix can be extremely ill-conditioned for typical plasmas unless the frequency is pre-scaled, otherwise the zero singular values (to within roundoff) will not be clearly delineated from the non-zero singular values. This is done by scaling  $s$  such that  $\hat{s} = s/k$ , where  $k$  is chosen heuristically such that the roots of the characteristic polynomial are approximately less than 1. After the realization procedure yields the scaled matrices  $\hat{A}$ ,  $\hat{B}$ ,  $\hat{C}$ , and  $\hat{D}$ , the actual matrices can be found by unscaling as  $A = k\hat{A}$ ,  $B = k\hat{B}$ ,  $C = \hat{C}$ , and  $D = \hat{D}$ .

[17] The minimal polynomial of this system (with no cancellation)  $m(s)$  is

$$m(s) = (s + \nu)(s^2 + 2s\nu + \nu^2 + |\omega_c|^2) = d(s) \quad (18)$$

[18] This technique converts the frequency domain description of a cold plasma to a set of first-order differential equations, one set for each point in the space. The resulting system is in semi-discrete form, that is, a first-order ODE over a large number of spatial points, where we have collected all the unknowns as a single vector  $\mathbf{u}$ :

$$\frac{\partial \mathbf{u}}{\partial t} = f(\mathbf{u}) \quad (19)$$

To solve the full system, then, we solve the above ODE with any suitable time stepping scheme, e.g., Runge–Kutta. We can also apply the same techniques to other general, linear material. One particularly useful application of the technique in a computational setting is to the perfectly matched layer (PML), which we discuss next.

### 2.4. Application to the Perfectly Matched Layer

[19] Numerical simulation spaces must be truncated by appropriate boundary conditions. Naive truncations, e.g., setting some fields to zero at the boundary, are perfectly reflecting, which is only useful for a limited number of computational problems. More typically for wave propagation problems, the boundary is truncated with some form of radiation boundary or absorbing boundary condition. The perfectly matched layer (PML) is one such absorbing boundary. The PML is normally formulated in one of two ways, either as a stretching transformation on the curl operator [Chew and Weedon, 1994; Roden and Gedney, 2000; Chevalier and Inan, 2004] or as a modification of the material permittivity and permeability [Gedney, 1996; Teixeira and Chew, 1998]. We choose the latter: we start with a PML permeability and permittivity and show how to derive the equivalent conductivity. As shown by Teixeira and Chew [1998], a PML can be constructed for any dispersive, anisotropic material by applying a stretching transform on the material tensors  $\epsilon(s)$  and  $\mu(s)$ :

$$\begin{aligned} \epsilon_{\text{pml}}(s) &= \epsilon_0 \frac{1}{\det S} S \epsilon_r S \\ \mu_{\text{pml}}(s) &= \mu_0 \frac{1}{\det S} S \mu_r S \end{aligned} \quad (20)$$

The matrix  $S$  is defined as

$$S = \begin{bmatrix} \eta_x^{-1} & 0 & 0 \\ 0 & \eta_y^{-1} & 0 \\ 0 & 0 & \eta_z^{-1} \end{bmatrix} \quad (21)$$

To illustrate the technique, we now consider truncating a simple (non-anisotropic, nondispersive) material. Extension to truncation of a non-simple material follows straightforwardly. For a simple material, the PML reduces to the familiar UPML [Gedney, 1996]:

$$\begin{aligned} \epsilon_{\text{pml}}(s) &= \epsilon_0 \epsilon_r \hat{S} \\ \mu_{\text{pml}}(s) &= \mu_0 \mu_r \hat{S} \\ \hat{S} &= \begin{bmatrix} \eta_x^{-1} \eta_y \eta_z & 0 & 0 \\ 0 & \eta_x \eta_y^{-1} \eta_z & 0 \\ 0 & 0 & \eta_x \eta_y \eta_z^{-1} \end{bmatrix} \end{aligned} \quad (22)$$

There is some flexibility in the choice of the stretching parameters  $\eta_x$ ,  $\eta_y$ , and  $\eta_z$ . They are normally chosen such that the wave is damped in the direction normal to a given boundary, e.g., if  $\hat{x}$  is normal to the boundary, then  $\eta_y = \eta_z = 1$  and  $\eta_x$  is a complex, frequency-dependent damping term. Two or three of these terms will be nonunity in a corner, depending on whether two or three faces meet. In this paper, we use the complex frequency-shifted PML (CFS-PML). Here  $\sigma_i^*$  is the PML loss term, which is not the same as the equivalent dispersive conductivities  $\sigma_{\text{pml}}(s)$  and  $\sigma_{m,\text{pml}}(s)$  we derive below. The subscript  $i$  denotes one of the principal directions  $x$ ,  $y$ , or  $z$ .

$$\eta_i = 1 + \frac{\sigma_i^*}{\alpha_i + s\epsilon_0} = \frac{s + \left(\frac{\alpha_i + \sigma_i^*}{\epsilon_0}\right)}{s + \frac{\alpha_i}{\epsilon_0}} \quad (23)$$

For convenience, we define the parameters  $\beta_i = (\alpha_i + \sigma_i^*)/\epsilon_0$  and  $\gamma_i = \alpha_i/\epsilon_0$  so that

$$\eta_i = \frac{s + \beta_i}{s + \gamma_i} \quad (24)$$

To use the scheme described above, we must convert this into an equivalent conductivity. The equivalent electric and magnetic conductivity is

$$\begin{aligned} \sigma_{\text{pml}} &= \epsilon_0 \epsilon_r s (\hat{S} - I) \\ \sigma_{m,\text{pml}} &= \mu_0 \mu_r s (\hat{S} - I) \end{aligned} \quad (25)$$

Explicitly,  $G(s) = s(\hat{S} - I)$  is

$$\begin{aligned} G(s) &= \begin{bmatrix} g_{xx} & 0 & 0 \\ 0 & g_{yy} & 0 \\ 0 & 0 & g_{zz} \end{bmatrix} \\ g_{xx}(s) &= s \left( \frac{(s + \gamma_x)(s + \beta_y)(s + \beta_z)}{(s + \beta_x)(s + \gamma_y)(s + \gamma_z)} - 1 \right) \\ g_{yy}(s) &= s \left( \frac{(s + \beta_x)(s + \gamma_y)(s + \beta_z)}{(s + \gamma_x)(s + \beta_y)(s + \gamma_z)} - 1 \right) \\ g_{zz}(s) &= s \left( \frac{(s + \beta_x)(s + \beta_y)(s + \gamma_z)}{(s + \gamma_x)(s + \gamma_y)(s + \beta_z)} - 1 \right) \end{aligned} \quad (26)$$

A DG domain need not necessarily be aligned along the principal axes; as such, it is often useful to construct a PML that absorbs waves incident on boundaries that are tilted with respect to one of the primary axes. This case can be handled by a simple rotation of the fields into a reference frame such that one of the scaling factors ( $\eta_x$ ,  $\eta_y$ , or  $\eta_z$ ) is normal to the boundary in that frame. In other words, suppose the PML equivalent currents are governed by the following ODE:

$$\begin{aligned} \mathbf{x}' &= A\mathbf{x} + B\mathbf{E} \\ \mathbf{J}_{\text{pml}} &= C\mathbf{x} + D\mathbf{E} \end{aligned} \quad (27)$$

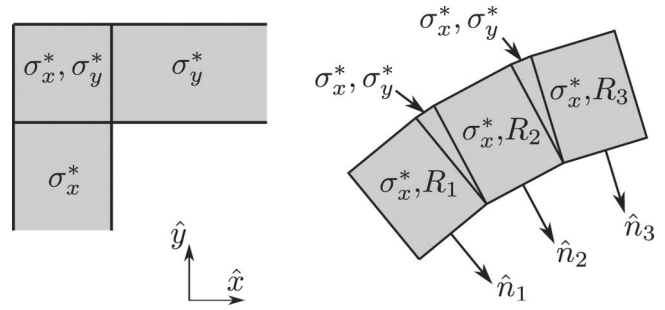


**Figure 1.** (left) Diagram of a right-angle PML termination. The mesh conforms to the perfectly matched layer (PML) boundary (shaded). The loss terms are set such that  $\sigma_x^*$  is active at faces where  $\hat{x}$  is normal to the boundary and  $\sigma_y^*$  is active where  $\hat{y}$  is normal. Both  $\sigma_x^*$  and  $\sigma_y^*$  are used in the corner. (right) The same for a quasi-circular domain. Within each rectangle, we use a base PML with only the  $\sigma_x^*$  component set ( $\sigma_y^* = \sigma_z^* = 1$ ), then rotate as in equation (28) so the face normal interior to the domain points in the  $\hat{x}$  direction. Each normal  $\hat{n}_i$  has a corresponding rotation matrix  $R_i$ . In the wedges at the corners in between each rectangle, we set  $\sigma_x^* = \sigma_y^*$  and  $\sigma_z^* = 1$ , which is invariant under rotations about the  $\hat{z}$  axis and so is identical for all wedges.

Given a rotation matrix  $R$  that performs this transformation, the rotated system is

$$\begin{aligned} A' &= A \\ B' &= BR \\ C' &= R^T C \\ D' &= R^T D \end{aligned} \quad (28)$$

### 3. Verification

[20] We now demonstrate the validity of the techniques described in section 2 on two model problems, a cold plasma and a PML. In the case of the PML, we show that the technique converges, that is, the reflection error decreases as a function of the polynomial order of the DG scheme (equivalently, the number of interpolation points per unit length within the boundary). For the cold plasma, we demonstrate that the scheme shows the correct wave modes expected from analytical cold plasma theory.

#### 3.1. PML

[21] The PML is tested on a rectangular two-dimensional free space domain surrounded by an absorbing buffer layer. We use Gmsh [Geuzaine and Remacle, 2009] to mesh the domain into 2400 triangles. The mesh conforms to the PML boundary, that is, the boundary between the main computational domain and the PML is flat, as illustrated in Figure 1 (left). A sinusoidal current source is placed at the center of the domain and the simulation is run for sufficient time for reflections to completely fill the computational domain. A second simulation is run with an identical inner mesh, but twice as large, which serves as a reference solution. We vary the polynomial order  $N$  of the scheme and plot the final normalized reflection error in dB as a function of the PML

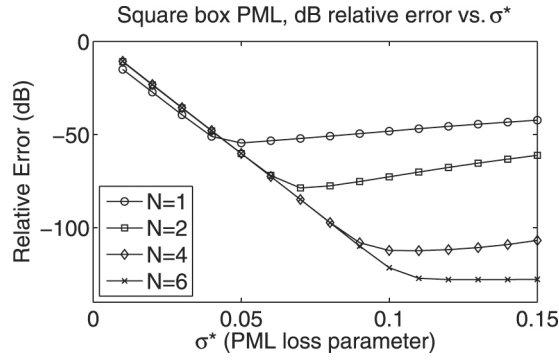


**Figure 2.** Reflection error for a PML terminating a square domain. We plot the error in dB relative to a reference simulation, that is,  $20 \log_{10}(|E_z - E_{z,ref}|/|E_{z,ref}|)$ . The simulation is repeated for varying polynomial orders  $N$ . The reduction in error as a function of the polynomial order is roughly exponential as expected until  $N = 6$ , where finite precision effects limit the minimum achievable reflection error.

loss term  $\sigma^*$  (Figure 2). The normalized reflection error is the ratio of the normed magnitude of the error divided by the normed magnitude of the reference field, all within the region truncated by the PML. The scheme has comparable performance to PMLs implemented in FDTD, achieving reflection errors of less than  $-100$  dB for  $N > 2$ . We note that we use no grading of the PML loss term, as is commonly done in FDTD implementations – the PML is encountered by the wave as a single abrupt step in the material parameters. Grading is generally unnecessary in the DG scheme because of the stronger handling of material and field discontinuities as compared to FDTD. The realization approach can also be adapted to arbitrary curved boundaries. We discretize a circular domain with an off-center source. The PML is handled by segmenting the boundary into a discrete number of rectangles with  $90^\circ$  corners, as shown in Figure 1 (right). In the corner regions in between rectangles, we set both  $\sigma_x^* = \sigma_y^* = \sigma^*$ , where  $\sigma^*$  is some value that we allow to vary for the convergence tests. We note that if both  $\sigma_x^*$  and  $\sigma_y^*$  are set and equal to each other, the resulting material will remain invariant under rotations about the  $\hat{z}$  axis, so no other special handling is required for these corner

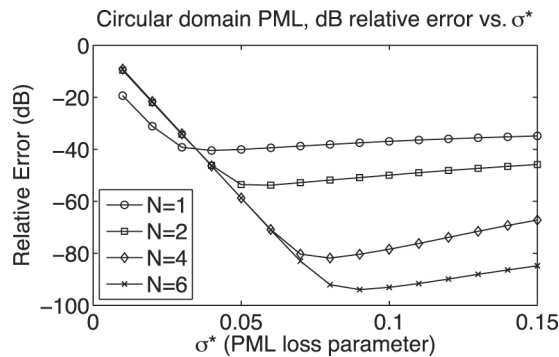


**Figure 3.** Reflection error for a PML terminating a circular domain. Plotted parameters are the same as those plotted in Figure 2.

regions. The convergence properties, plotted in Figure 3, are similar to those shown in Figure 2, with maximum reflection minimum errors less than  $-90$  dB.

### 3.2. Plasma

[22] We verify the plasma implementation by comparing a simulated dispersion relation to the theoretical dispersion relation. We use a cold electron plasma with gyrofrequency approximately equal to 600 kHz ( $B_0 \approx 21600$  nT) and a plasma frequency of 568 kHz ( $N_0 = 4000$  cm $^{-3}$ ), values typical of a midlatitude ionospheric plasma at approximately 200 km altitude. We mesh a one-dimensional domain 80 kilometers in length into 4000 finite elements. At 20 meters per element, this more than adequately resolves all wavelengths of primary interest (those with wave frequencies below approximately two times the plasma frequency). We “ping” the domain with a very short current pulse, a short differentiated Gaussian in time and a narrow Gaussian window in space.

[23] We then run the simulation and record all fields as a function of space and time. Two-dimensional Fourier transforming the fields and computing the magnitude of the complex Poynting flux yields an experimental dispersion diagram, which we plot in Figure 4 as a function of wave frequency  $\omega$  and wave number  $k$ . Allowed modes of the system show up as bright lines in this plot. We show both the measured and theoretical results for propagation parallel to the background magnetic field ( $\mathbf{k} \parallel \mathbf{B}_0$ ) and for

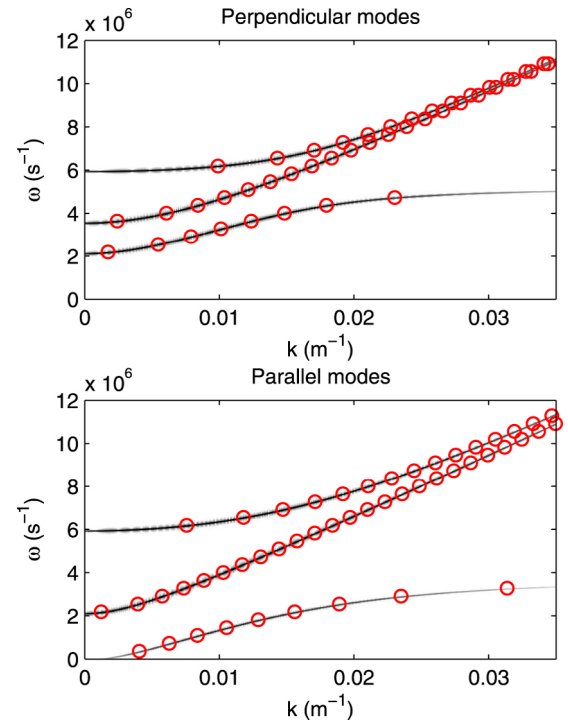


**Figure 4.** Simulated plasma dispersion diagram plotted as a function of wave frequency  $\omega$  and wave number  $k$ . The locations of the roots of the expected theoretical modes are plotted as superimposed circles. The plasma modes for (top) propagation perpendicular to the background magnetic field and (bottom) parallel propagation.



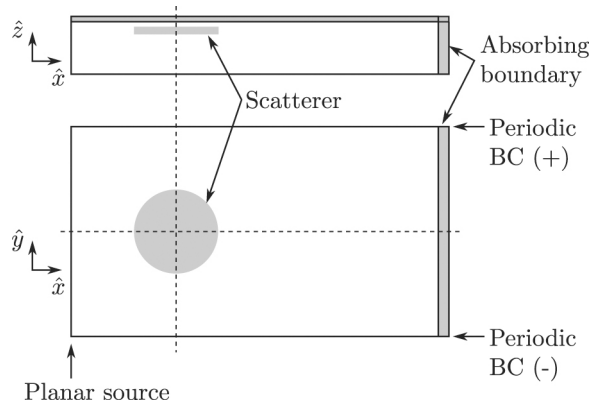


**Figure 5.** Diagram of the simulation domain for the VLF scattering problem, front and side view. The scatterer is located at position  $x = 0$ ,  $y = 0$ . Absorbing boundaries are placed at the top and end of the domain. A waveguide mode (or multiple modes) propagating in the  $+\hat{x}$  direction is sourced at the input plane indicated. The boundaries in the transverse direction are periodic.

perpendicular ( $\mathbf{k} \perp \mathbf{B}_0$ ) propagation. The theoretical dispersion relation is superimposed on this plot as circles.

[24] The scheme shows excellent agreement with theory, with the propagating wave modes gradually dissipating as the wave number grows very large and can no longer be adequately resolved by the DG mesh.

#### 4. Scattering Model

[25] We now apply the DG technique described above to a three-dimensional scattering problem in the Earth-ionosphere waveguide. Waves radiated by an antenna at VLF frequencies (3–30 kHz) are effectively guided between the ground and the conductive lower ionosphere and propagate efficiently over very long distances with modal attenuation rates of only a few dB per megameter [Davies, 1990, p. 367]. Assuming a smooth ionosphere, the mode excitation factors and attenuation rates can be computed as described by Lehtinen and Inan [2008, 2009] and Lehtinen et al. [2010]. The modal structure is relatively simple at large distances from the antenna with the bulk of the contributions to the Poynting flux in the QTM1 and QTM2 modes [Lehtinen et al., 2010]. Any perturbation along this path, in the form of modified ground conductivity, electron density, or collision frequency, will scatter the incoming fields, potentially creating strong perturbations on the received signal amplitude of a coherent signal at a receiver some distance away from the transmitter.

##### 4.1. Simulation Domain

[26] We carry out the simulation on a box-shaped domain of size 900 km by 400 km on the ground and 100 km in height (Figure 5). We subdivide this domain into a number of horizontal layers (in order to enforce a conformal mesh) with layer thickness approximately proportional to the characteristic length scale in the medium, which we define as the wavelength of a whistler mode wave propagating parallel to the background magnetic field  $\mathbf{B}_0$ . We truncate the upper part of the domain with an absorbing boundary.

The “input” to the domain is a sum of plane wave sources at one face ( $x = -200$  km), extending from the ground up through the ionosphere. The waves propagate in the  $+\hat{x}$  direction, interacting with a scattering region in the ionosphere centered at  $(x = 0, y = 0)$ , propagating forward and finally terminating at another absorbing boundary placed at  $x = 700$  km. To avoid numerical difficulties with terminating very oblique waves, and since the bulk of the scattered wave energy is in the forward direction [Lehtinen et al., 2010], we use a periodic boundary condition along the  $\hat{y}$  dimension at  $y = -200$  km and  $y = 200$  km. We then mesh the domain using Gmsh [Geuzaine and Remacle, 2009], with average element size again proportional to the characteristic length scale, yielding a domain with approximately 2.5 million tetrahedrons. On each tetrahedron, the solution is expanded in an interpolating polynomial basis. The total number of interpolation points per tetrahedron is dependent on the order of this polynomial basis; for instance, for a second-order polynomial basis ( $N = 2$ ), we have  $(N + 1)(N + 2)(N + 3)/6 = 10$  points per element. For the fourth order results in this paper, this increases to 35 points per element, for a total of  $\sim 87$  million unknowns per field.

##### 4.2. Plasma Parameters

[27] The background number density, collision frequency, and magnetic field are as described by Lehtinen et al. [2010]. Because of the enormous computational cost associated with a full 3-D simulation, we restrict ourselves to a small number of test cases. In particular, we restrict ourselves to scattering from ionospheric disturbances created by relatively large lightning discharges. We use the lightning discharge cases described by Marshall et al. [2010] and Lehtinen et al. [2010]. For context, in Figure 6 we show the ambient electron density and the height-integrated change in the electron density distribution for two of the strong discharges considered by Marshall et al. [2010]. The “40V” case refers to the density perturbation induced by a large, vertically-oriented lightning discharge. The number 40 refers to the  $E_{100}$  parameter. The 10H case refers to a horizontally-oriented intercloud, multiple stroke (60 discharges in total)

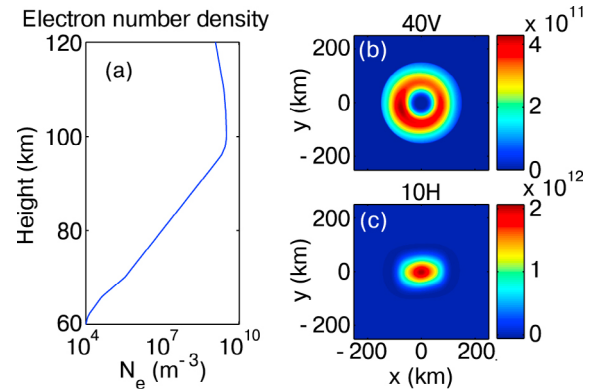


**Figure 6.** (a) The ambient electron density as a function of altitude. (b) Height-integrated electron density perturbation in  $\text{m}^{-2}$  for a single vertical lightning discharge with  $E_{100} = 40$  V/m. (c) Height-integrated electron density perturbation for 60 horizontal discharges with  $E_{100} = 10$  V/m.



lightning discharge with  $E_{100} = 10$  V/m. The 60 stroke, 10H case is not necessarily physical but is used to establish an upper bound on the magnitude of the scattered field because of lightning EMP-induced ionization under the best possible conditions. The background magnetic field is taken to be

$$\mathbf{B}_0 = |B_0|(\cos \theta \sin \phi \hat{\mathbf{x}} + \sin \theta \cos \phi \hat{\mathbf{y}} + \cos \phi \hat{\mathbf{z}}), \quad (29)$$

where  $|B_0| = 5 \times 10^{-5} T$ ,  $\phi = 45^\circ$ , and  $\theta = 270^\circ$ .

### 4.3. Incident Source

[28] Since we are computing the scattered field from a narrowband transmitter some large distance away ( $> 1$  Mm) from the scatterer we are modeling, it is more efficient to use an approximate method to propagate the fields from a VLF transmitter in the Earth-ionosphere waveguide out to some distance, then use the field amplitudes at that distance as our incident source. The method we use is a modal technique described by *Lehtinen et al.* [2010]. The method uses a full-wave method to compute a set of height gains (that is, the mode structure as a function of altitude) and mode amplitudes at some arbitrary distance from a vertical dipole source. At the scatterer, we assume the cylindrical wavefronts are quasi-planar and then compute a set of equivalent source currents for the given mode (or sum of modes) along a large plane (shown in Figure 5) on one side of the domain, where  $\hat{\mathbf{n}}$  is the normal to the incident source plane, using the convention that the waves propagate in the same half plane as  $\hat{\mathbf{n}}$ :

$$\begin{aligned} J_s &= \hat{\mathbf{n}} \times H \\ M_s &= -\hat{\mathbf{n}} \times E \end{aligned} \quad (30)$$

As observed by *Lehtinen et al.* [2010], the dominant contributions at large distances from the VLF source are in the quasi-TM1 (QTM1) and QTM2 modes. For this study, we separately compute the scattered fields for the QTM1 and QTM2 modes, then repeat the computation for the full mode sums at some fixed distances (1 Mm, 2 Mm, and 3 Mm) from the transmitter. We use the full mode sums because the presence of modal nulls can significantly affect the apparent magnitude of the scattered field from a fixed reference point on the ground [*Marshall and Inan*, 2010], an important factor to consider when drawing conclusions from an amplitude and phase measurement at a single VLF receiver.

## 5. Results

[29] We apply our model to a number of representative test cases, two pure waveguide modes and mode sums at three distances. Each simulation is parallelized across 48 CPU cores using the Petsc MPI library [*Balay et al.*, 1997, 2010, PETSc Web page, <http://www.mcs.anl.gov/petsc>]. The simulation is run until convergence (approximately 4 ms). The domain is partitioned across CPUs using ParMETIS [*Karypis et al.*, 1997] in order to minimize communication between nodes. Each node computes its local matrix-vector products using an accelerated BLAS library. Inter-node communication is done via generic vector scatters in the Petsc library. Since each simulation requires on the order of 1000 CPU hours, we limit our study to a relatively small number of illustrative cases.

[30] We first simulate two simple pure-mode cases. For a relatively smooth ionosphere and far from the source, the bulk of the wave power will be in the QTM1 and QTM2 modes, so we consider these two modes separately. We simulate scattering from these pure modes for two large vertical lightning discharges ( $E_{100} = 30$  V/m and  $E_{100} = 40$  V/m) and two multiple-stroke, horizontal intercloud discharges (60 flashes at  $E_{100} = 7$  V/m and  $E_{100} = 10$  V/m [*Marshall et al.*, 2008; *Marshall and Inan*, 2010]). The vertical discharge creates a flattened ring-shaped disturbance, peaking between 80 and 90 km altitude, while the horizontal discharges create very localized, oval-shaped disturbances. We source an incident QTM1 or QTM2 mode at one end of the domain and run the simulation until steady state is reached. Equivalent complex fields are computed by finding the sine and cosine parts, found by advancing the steady state simulation results one quarter wavelength in time at the transmitter frequency (24 kHz). We compute a reference simulation without an ionospheric disturbance and use this to compute the field difference (in dB) and (unwrapped) phase:

$$\Delta A_{\text{scattered}} = 20 \log_{10} \frac{|E_{\text{perturbed}}|}{|E_{\text{ref}}|} \quad (31)$$

$$\Delta \phi_{\text{scattered}} = \angle(E_{\text{ref}}) - \angle(E_{\text{perturbed}}) \quad (32)$$

We also compute the pure scattered field referenced to the reference field as

$$\left| \frac{E_{\text{scattered}}}{E_{\text{ref}}} \right| = \left| \frac{E_{\text{ref}} - E_{\text{perturbed}}}{E_{\text{ref}}} \right| \quad (33)$$

[31] The amplitude and phase perturbations for the vertical 40 V/m and 60-stroke horizontal 10 V/m discharges are shown in Figure 7 for an incident QTM1 mode. We also show the pure scattered field amplitudes in dB, normalized to the reference field, in Figure 8. The results are similar to those of *Lehtinen et al.* [2010, Figure 5], but with a larger amplitude because of the larger magnitude of the disturbance. The peak amplitude perturbation for the 40 V/m case is approximately 0.05 dB, with a phase perturbation of  $0.4^\circ$ . The horizontal discharge case is larger, on the order of 0.2 dB with a maximum phase perturbation of approximately  $2^\circ$ . The 30 V/m vertical and multiple-stroke 7 V/m horizontal cases (not shown) have similar qualitative shapes but smaller perturbation magnitudes on the order of 0.02 dB for the vertical discharge and 0.04 dB for the horizontal discharge. The QTM2 cases (again, not shown), are also qualitatively quite similar but larger in magnitude, a more measurable 0.25 dB maximum for the vertical 40 V/m discharge ( $1.5^\circ$  in phase) and 0.8 dB for the 60-flash horizontal 10 V/m discharge ( $6^\circ$  in phase).

[32] Most striking is the extreme spatial variation in the magnitude of the scattered field, particularly for the case of the ring-shaped disturbance produced by a vertical discharge, where the distance from the strongest peak to a null in the scattered field is on the order of 50 km. Also of particular note is the phase response. To the authors' knowledge, this is the first full plot of the phase response to scattering from an intense lightning EMP-induced ionospheric disturbance. Most studies of "early" VLF events thus

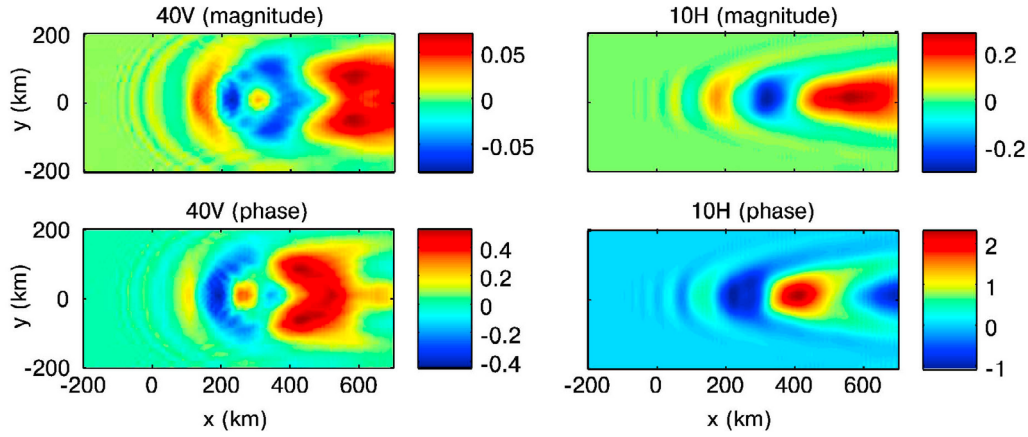


**Figure 7.** Scattered field difference  $\Delta A$  and  $\Delta\phi$  for a 24 kHz QTM1 waveguide mode incident on a lightning-induced electron density irregularity. (left) The scattered fields (vertical electric field at the ground) in dB magnitude and degrees phase for a large vertical lightning discharge with magnitude  $E_{100} = 40$  V/m. (right) The same for 60 consecutive horizontal discharges, each with magnitude  $E_{100} = 10$  V/m.

far focused primarily on the magnitude response on a received VLF narrowband signal. Noting, however, that for these simple single-mode cases, the phase response exhibits strong peaks where there is a null in the magnitude response (and vice versa), the phase response to a lightning EMP-induced density perturbation might also be a useful quantity to consider.

[33] For our second set of trials, we use the full mode sums for a VLF transmitter located at some distance from the ionospheric disturbance. As noted by *Marshall and Inan* [2010], the presence of modal nulls can significantly alter the magnitude of observed VLF scattered field. As such, we conduct six additional trials for strong scatterers located at fixed distances of 1 Mm, 2 Mm, and 3 Mm from a VLF transmitter. The intent of these trials is to show the shape of the scattered field under more realistic (multimode) conditions and to demonstrate that scattered fields with very complicated spatial structure can occur for some configurations, particularly when many waveguide modes are present. The results are summarized in Figure 9, plotted as the change in amplitude in dB in the vertical electric field as measured on the ground. We also show the pure scattered field amplitudes in dB, normalized to the reference field, in Figure 10. For reference, we show the background electric field in Figure 11. The horizontal discharges show relatively

less transverse variation in the shape of the scattered field, so 2-D simulations with cylindrical symmetry could provide reasonable estimates to these scattered fields. The vertical discharges, however, again show strong transverse variation. At larger distances, the QTM1 and QTM2 modes begin to dominate and the scattered fields begin to more closely resemble the single-mode scattering patterns in Figure 7. We note that this idealized model assumes perfect uniformity along the path from the transmitter to the lightning-induced plasma perturbation. In reality, additional modes may be present because of unmodeled density irregularities or variations in the ground conductivity along the path, leading to slightly stronger scattered field values than would be expected from a pure mode QTM1 case. For full mode sums, typical maximum scattered field amplitudes are greater than 0.2 dB for the cases considered, both for the intense vertical discharge and the multistroke horizontal discharge. Given the amplitude variation and angular beam width, we can say that scattering from lightning-induced electron density perturbations may be consistent with some observations of “early” VLF events; however, artificially large or multiple discharges are required to produce very large amplitude changes. Additionally, without exact knowledge of the exact mode structure (in the presence of unmodeled variations in the ambient electron density along the path), it is not

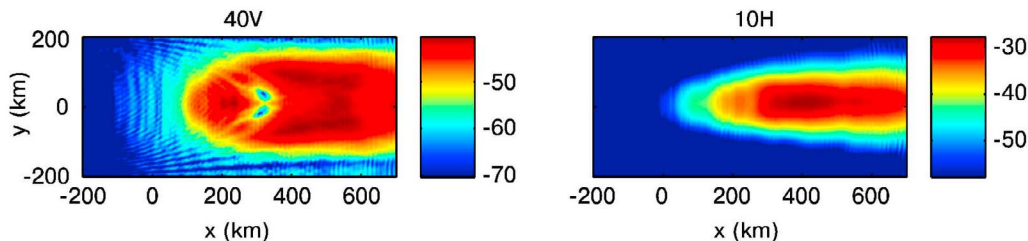


**Figure 8.** Same data as Figure 7, but showing only the pure scattered field magnitude in dB with respect to the reference field,  $20 \log_{10} |E_{\text{scattered}}/E_{\text{ref}}|$  (from equation (33)). The plot range is fixed at 30 dB for each plot, with the maximum set to the maximum scattering amplitude.

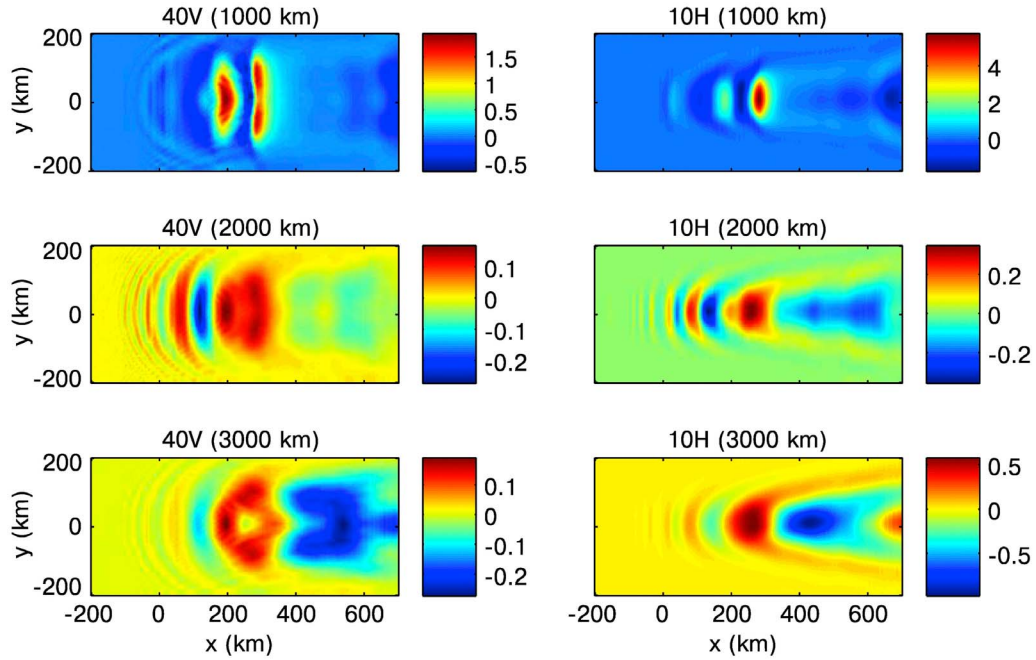


**Figure 9.** Amplitude perturbation (dB change in the magnitude of the vertical electric field as measured on the ground) for a disturbance located at a distance from a 24 kHz transmitter. The incident, multimode wavefield is sourced at the leftmost plane. (left) A vertical lightning discharge with  $E_{100} = 40$  V/m (a ring-shaped disturbance). (right) The same but for 60 horizontal, intercloud discharges with  $E_{100} = 10$  V/m. We plot three cases for perturbations located at 1, 2, and 3 Mm distance from a vertical VLF antenna. The 1000 km case shows artificially high scattering amplitudes due to the presence of modal nulls at approximately 180 and 280 km from the scatterer.

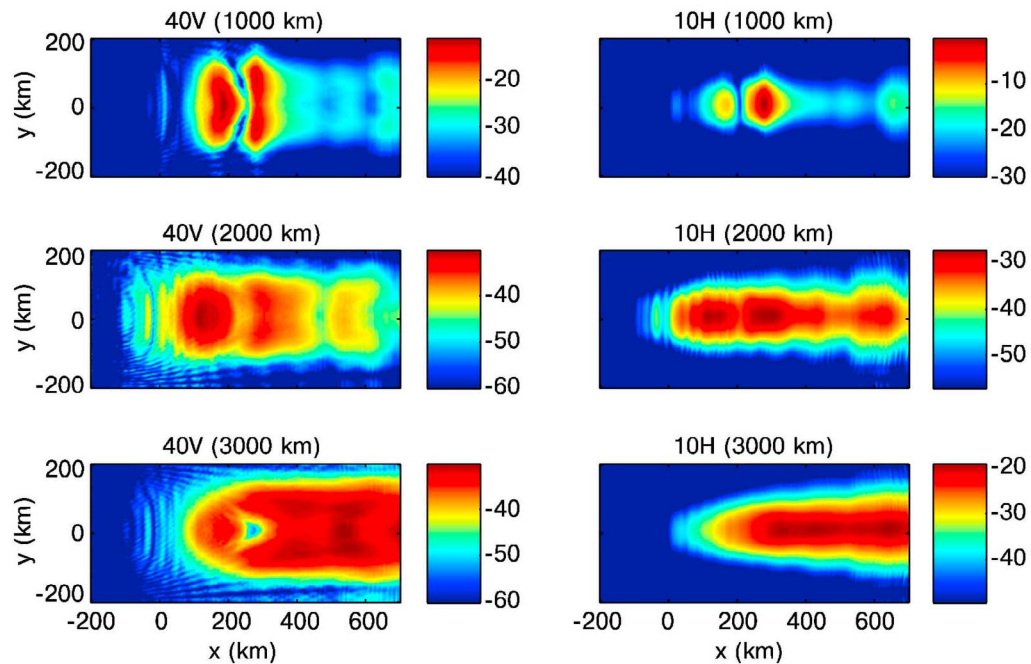


**Figure 10.** Same data as Figure 9, but showing only the pure scattered field magnitude in dB with respect to the reference field,  $20 \log_{10}|E_{\text{scattered}}/E_{\text{ref}}|$  (from equation (33)). The plot range is fixed at 30 dB for each plot, with the maximum set to the maximum scattering amplitude.

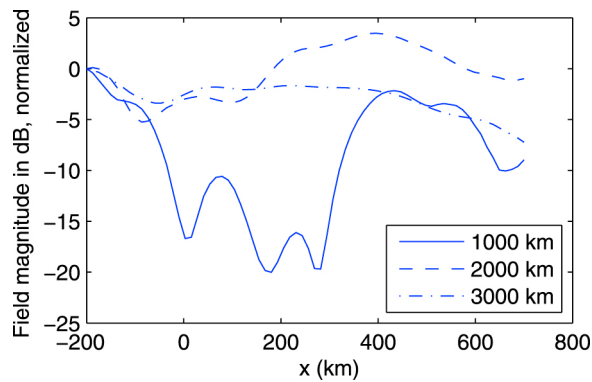


**Figure 11.** Vertical reference electric field magnitude as observed on the ground for the cases shown in Figure 9, normalized to their values at  $x = -200$  km, plotted for scatterers located at 1000, 2000, and 3000 km from the transmitter. Two nulls are visible in the 1000 km case, but the other cases are smooth.

possible to make extremely strong inferences about the precise shape and magnitude of the scatterer from a single ground-based measurement.

## 6. Conclusions

[34] We have described a technique for automating the incorporation of any dispersive, anisotropic material in the discontinuous Galerkin (DG) framework. We have demonstrated how the technique can be applied to simulating magnetized plasmas and the perfectly matched layer (PML) on curved domains, showing the correctness and flexibility of the approach.

[35] As an application of the technique, we modeled a practical problem: scattering of VLF wave energy from lightning EMP-induced ionospheric disturbances. Since the DG technique is easily adapted to use on unstructured grids, it is well-suited to simulating propagation in strongly inhomogeneous domains, such as at VLF frequencies in the Earth-ionosphere waveguide. Using a grid with finer sampling only where it is required, e.g., near the VLF reflection height ( $\sim 85$  km at night) allows the accurate simulation of domains much larger than that currently possible using low-order techniques on structured grids. Further, the technique is not limited to small scattered field amplitudes as in Born approximation approaches [Lehtinen et al., 2010].

[36] Using physically based models, we have shown that the spatial structure of the VLF scattered field from a lightning EMP-induced ionospheric disturbance can be quite complicated, showing rapid variations in the phase and amplitude over a scale of tens to hundreds of kilometers. These simulations demonstrate that scattering from such perturbations may produce amplitude changes of over 0.2 dB under smooth ambient conditions, consistent with results from the 2-D modeling of Marshall and Inan [2010]. However, even an intense single lightning stroke does not consistently produce scattered field amplitudes large enough to be consistent with all observations of “early” VLF events. In addition, the strong spatial variability in the scattered field and its dependence on ambient conditions further suggests that while some scattering of VLF transmitter signals due

to lightning discharges is commonplace, the likelihood of making successful observations of such an event via amplitude and phase measurements of a received narrowband VLF transmitter signal is strongly dependent on the position of the receiver relative to the induced perturbation and the transmitter. The bulk of the scattered wave energy is in the direction forward of the perturbation, but the fine-scale structure can be complicated, particularly when signal amplitudes are measured within 700 km of the perturbation. We have further shown that the phase response may also be an important factor to consider when measuring field perturbations from lightning-induced density perturbations.

[37] **Acknowledgments.** The authors were supported by the Office of Naval Research under prime award N000140710789 to the University of Maryland with subcontract Z882802 to Stanford and under grant N00014-09-1-0034-P00003 from the National Science Foundation under award 0636928 and by the Defense Threat Reduction Agency (DTRA) under grant HDTRA1-10-1-0115.

[38] Robert Lysak thanks the reviewers for their assistance in evaluating this paper.

## References

- Antsaklis, P. J. (1997), *Linear Systems*, edited by P. J. Antsaklis and A. N. Michel, McGraw-Hill, New York.
- Armstrong, W. C. (1983), Recent advances from studies of the trimpi effect, *Antact. J. U. S.*, 18, 281–283.
- Balay, S., W. D. Gropp, L. C. McInnes, and B. F. Smith (1997), Efficient management of parallelism in object oriented numerical software libraries, in *Modern Software Tools in Scientific Computing*, edited by E. Arge, A. M. Bruaset, and H. P. Langtangen, pp. 163–202, Birkhäuser, Boston, Mass.
- Balay, S., et al. (2010), PETSc users manual, revision 3.1, *Tech. Rep. ANL-95/11*, Argonne Natl. Lab., Argonne, Ill.
- Berenger, J.-P. (1994), A perfectly matched layer for the absorption of electromagnetic waves, *J. Comput. Phys.*, 114, 185–200, doi:10.1006/jcph.1994.1159.
- Chen, C.-T. (1999), *Linear System Theory and Design*, Oxford Univ. Press, New York.
- Cheng, Z., and S. A. Cummer (2005), Broadband VLF measurements of lightning-induced ionospheric perturbations, *Geophys. Res. Lett.*, 32, L08804, doi:10.1029/2004GL022187.
- Cheng, Z., S. A. Cummer, H.-T. Su, and R.-R. Hsu (2007), Broadband very low frequency measurement of D region ionospheric perturbations caused by lightning electromagnetic pulses, *J. Geophys. Res.*, 112(A11), A06318, doi:10.1029/2006JA011840.
- Chevalier, M. W., and U. S. Inan (2004), A PML using a convolutional curl operator and a numerical reflection coefficient for general linear media, *IEEE Trans. Antennas Propag.*, 52, 1647–1657, doi:10.1109/TAP.2004.831318.
- Chew, W. C., and W. H. Weedon (1994), A 3D perfectly matched medium from modified Maxwell’s equations with stretched coordinates, *Micro-wave Opt. Technol. Lett.*, 7, 599–604.
- Cummer, S. A. (2000), Modeling electromagnetic propagation in the Earth-ionosphere waveguide, *IEEE Trans. Antennas Propag.*, 48, 1420–1429, doi:10.1109/8.898776.
- Davies, K. (1990), *Ionospheric Radio*, Inst. of Electr. Eng., London.
- Gedney, S. D. (1996), An anisotropic perfectly matched layer-absorbing medium for the truncation of FDTD lattices, *IEEE Trans. Antennas Propag.*, 44, 1630–1639, doi:10.1109/8.546249.
- Geuzaine, C., and J.-F. Remacle (2009), Gmsh: A 3-D finite element mesh generator with built-in pre- and post-processing facilities, *Int. J. Numer. Methods Eng.*, 79(11), 1309–1331.
- Gilbert, E. (1963), Controllability and observability in multivariable control systems, *SIAM J. Control*, 2(1), 128–151.
- Hesthaven, J. S., and T. Warburton (2002), Nodal high-order methods on unstructured grids I. Time-domain solution of Maxwell’s equations, *J. Comput. Phys.*, 181, 186–221, doi:10.1006/jcph.2002.7118.
- Hesthaven, J. S., and T. Warburton (2007), *Nodal Discontinuous Galerkin Methods: Algorithms, Analysis, and Applications*, Springer, New York.
- Ho, B., and R. Kalman (1966), Effective construction of linear state-variable models from input–output functions, *Regelungstechnik*, 14(12), 545–592.

- Inan, U. S., T. F. Bell, and J. V. Rodriguez (1991), Heating and ionization of the lower ionosphere by lightning, *Geophys. Res. Lett.*, **18**, 705–708, doi:10.1029/91GL00364.
- Inan, U. S., S. A. Cummer, and R. A. Marshall (2010), A survey of ELF and VLF research on lightning-ionosphere interactions and causative discharges, *J. Geophys. Res.*, **115**, A00E36, doi:10.1029/2009JA014775.
- Johnson, M. P., U. S. Inan, S. J. Lev-Tov, and T. F. Bell (1999), Scattering pattern of lightning-induced ionospheric disturbances associated with early/fast VLF events, *Geophys. Res. Lett.*, **26**, 2363–2366, doi:10.1029/1999GL900521.
- Karypis, G., K. Schloegel, and V. Kumar (1997), ParMETIS 1.0: Parallel graph partitioning and sparse matrix ordering library, Tech. Rep. TR-97-060, Dep. of Comput. Sci., Univ. of Minn., Minneapolis. [Available at <http://www.cs.umn.edu/~metis>.]
- Lehtinen, N. G., and U. S. Inan (2008), Radiation of ELF/VLF waves by harmonically varying currents into a stratified ionosphere with application to radiation by a modulated electrojet, *J. Geophys. Res.*, **113**, A06301, doi:10.1029/2007JA012911.
- Lehtinen, N. G., and U. S. Inan (2009), Full-wave modeling of transionospheric propagation of VLF waves, *Geophys. Res. Lett.*, **36**, L03104, doi:10.1029/2008GL036535.
- Lehtinen, N. G., R. A. Marshall, and U. S. Inan (2010), Full-wave modeling of early VLF perturbations caused by lightning electromagnetic pulses, *J. Geophys. Res.*, **115**, A00E40, doi:10.1029/2009JA014776.
- Marshall, R. A., and U. S. Inan (2010), Two-dimensional frequency domain modeling of lightning EMP-induced perturbations to VLF transmitter signals, *J. Geophys. Res.*, **115**, A00E29, doi:10.1029/2009JA014761.
- Marshall, R. A., U. S. Inan, and T. W. Chevalier (2008), Early VLF perturbations caused by lightning EMP-driven dissociative attachment, *Geophys. Res. Lett.*, **35**, L21807, doi:10.1029/2008GL035358.
- Marshall, R. A., U. S. Inan, and V. S. Glukhov (2010), Elves and associated electron density changes due to cloud-to-ground and in-cloud lightning discharges, *J. Geophys. Res.*, **115**, A00E17, doi:10.1029/2009JA014469.
- Moore, R., C. P. Barrington-Leigh, U. S. Inan, and T. F. Bell (2003), Early/fast VLF events produced by electron density changes associated with sprite halos, *J. Geophys. Res.*, **108**(A10), 1363, doi:10.1029/2002JA009816.
- Pappert, R. A., and J. A. Ferguson (1986), VLF/LF mode conversion model calculations for air to air transmissions in the Earth-ionosphere waveguide, *Radio Sci.*, **21**, 551–558, doi:10.1029/RS021i004p00551.
- Pasko, V. P., U. S. Inan, Y. N. Taranenko, and T. F. Bell (1995), Heating, ionization and upward discharges in the mesosphere due to intense quasi-electrostatic thundercloud fields, *Geophys. Res. Lett.*, **22**, 365–368, doi:10.1029/95GL00008.
- Pasko, V. P., U. S. Inan, and T. F. Bell (1998), Ionospheric effects due to electrostatic thundercloud fields, *J. Atmos. Sol. Terr. Phys.*, **60**, 863–870, doi:10.1016/S1364-6826(98)00022-4.
- Peter, W. B., M. W. Chevalier, and U. S. Inan (2006), Perturbations of mid-latitude subionospheric VLF signals associated with lower ionospheric disturbances during major geomagnetic storms, *J. Geophys. Res.*, **111**, A03301, doi:10.1029/2005JA011346.
- Roden, J. A., and S. D. Gedney (2000), Convolution PML (CPML): An efficient FDTD implementation of the CFS-PML for arbitrary media, *Microwave Opt. Technol. Lett.*, **27**(5), 334–339, doi:10.1002/1098-2760(20001205)27:5<334::AID-MOP14>3.0.CO;2-A.
- Schutter, B. D. (2000), Minimal state-space realization in linear system theory: An overview, *J. Comput. Appl. Math.*, **121**, 331–354.
- Schutter, B. D., and B. D. Moor (1995), Minimal state space realization of mimo systems in the max algebra, paper presented at Third European Control Conference, Eur. Union Control Assoc., Rome.
- Stix, T. H. (1962), *The Theory of Plasma Waves*, McGraw-Hill, New York.
- Taflove, A., and S. C. Hagness (2005), *Computational Electrodynamics: The Finite-Difference Time-Domain Method*, 3rd ed., Artech House, Norwood, Mass.
- Teixeira, F., and W. Chew (1998), General closed-form PML constitutive tensors to match arbitrary bianisotropic and dispersive linear media, *IEEE Microwave Guided Wave Lett.*, **8**(6), 223–225, doi:10.1109/75.678571.
- Uman, M. A., and D. K. McLain (1970), Lightning return stroke current from magnetic and radiation field measurements, *J. Geophys. Res.*, **75**, 5143–5147, doi:10.1029/JC075i027p05143.
- Yee, K. (1966), Numerical solution of initial boundary value problems involving Maxwell's equations in isotropic media, *IEEE Trans. Antennas Propag.*, **14**, 302–307, doi:10.1109/TAP.1966.1138693.

T. F. Bell, F. R. Foust, U. S. Inan, and M. Spasojevic, Department of Electrical Engineering, Stanford University, Packard Bldg., 350 Serra Mall, Stanford, CA 94305, USA. (ffoust@stanford.edu)